nances responsible for the jumps at 2.89 AU have not yet been identified by our team, although they may be associated with various secular resonances and the weak 6:1 mean motion resonance with Saturn.

26. D. Vokrouhlický, M. Brož, P. Farinella, Z. Knežević, *Icarus* **150**, 78 (2001).

27. We thank V. Carruba, L. Dones, D. Durda, Z. Knežević, H. Levison, F. Marzari, P. Michel, A. Milani, F. Namouni, F. Roig, and D. Rubincam as well as our anonymous referees, for valuable contributions. Our work was strongly inspired by P. Farinella, a leading Italian planetary scientist who championed the importance of the Yarkovsky effect before his untimely death on 25 March 2000. We gratefully acknowledge the computational resources provided by the Cornell Theory Center. Research funds were provided by NASA grants NAG5-8950 and NAG5-9082 and European Space Agency contract 14018/2000/F/TB.

2 October 2001; accepted 24 October 2001

Collisions and Gravitational Reaccumulation: Forming Asteroid Families and Satellites

Patrick Michel,[1]* Willy Benz,[2] Paolo Tanga,[1,3] Derek C. Richardson[4]

Numerical simulations of the collisional disruption of large asteroids show that although the parent body is totally shattered, subsequent gravitational reaccumulation leads to the formation of an entire family of large and small objects with dynamical properties similar to those of the parent body. Simulations were performed in two different collisional regimes representative of asteroid families such as Eunomia and Koronis. Our results indicate that all large family members must be made of gravitationally reaccumulated fragments; that the post-collision member size distribution and the orbital dispersion are steeper and smaller, respectively, than for the evolved families observed today; and that satellites form frequently around family members.

Observed asteroid families in the main asteroid belt are of collisional origin (*1*). More than 20 asteroid families have been identified, each corresponding to groups of bodies concentrated in proper orbital element space (*2*) and sharing similar spectral properties (*3*). The theory of the collisional origin of asteroid families rests entirely on these similarities in dynamical and spectral properties and not on the understanding of the collisional physics itself. Despite several attempts (*4*), numerical simulations of fragmentation, although reproducing laboratory experiments on centimeter scale, have not been able to simultaneously explain the dynamical properties and the mass spectrum of asteroid families (*5*, *6*).

Here we explicitly simulate both the fragmentation of a parent body and the evolution of the debris cloud to late times, typically several days after fragmentation. We show that gravitational interactions between fragments result in reaccumulations (Fig. 1) and lead to the formation of a family of bound aggregates (*7*). This cluster, composed of well-dispersed "rubble piles"' (*8*) of all sizes, eventually evolves into one of today's asteroid families.

In our simulations, we model the family parent bodies as monolithic basalt objects, even though it is likely that they would have been shattered by the numerous small impacts taking place before a dispersing event. However, before being dispersed, our parent bodies are also shattered and, because gravity dominates over mechanical strength at these scales, this happens at correspondingly low energy costs (*9*). Consequently, although the collisional outcome may change in the details, we do not believe that the internal structure of the parent bodies can prevent reaccumulation from occurring.

The outcome of the collision is computed with a three-dimensional smooth particle hydrodynamics (SPH) code (*10*). This code solves in a Lagrangian framework the usual conservation equations (mass, momentum, and energy) in which the stress tensor has a nondiagonal part. We use the Tillotson equation of state for basalt (*11*, *12*), which is computationally expedient while sophisticated enough to allow its application over a wide range of physical conditions. Plasticity is introduced by modifying the stresses beyond the elastic limit with a von Mises yielding relation. For the lower tensile stresses associated with brittle failure, we use a fracture model based on the nucleation of incipient flaws, whose number density is given by a Weibull distribution (*13*, *14*).

Once the collision is over and fractures cease to propagate, the hydrodynamic simulations are stopped and intact fragments are identified. Typically, for the collisions considered here, the bodies are totally shattered into fragments of mass equal to our mass resolution. This corresponds to boulder sizes of ≈1 to 4 km. These fragments and their corresponding velocity distributions are fed into a gravitational *N*-body code, which computes the evolution of the system over the following days.

Because we are dealing with a large number of bodies (up to 2×10^5) that we want to follow over long periods of time, we use a parallel *N*-body hierarchical tree code (*15*) to compute the dynamics. The tree component of the code provides a convenient means of consolidating forces exerted by distant particles, reducing the computational cost. The parallel component divides the work evenly among available processors, adjusting the load at each time step according to the amount of work done in the previous force calculation. The code uses a straightforward second-order leapfrog scheme for the integration and computes gravity moments from tree cells to hexadecapole order. Collisions are identified at each step with a fast neighbor-search algorithm.

In order to keep the calculations tractable, we made some simplifications. We assume perfect sticking, which means that all colliding fragments are forced to stick regardless of their relative velocities (*16*). This assumption is justified because the initial impact results in an overall expanding cloud of fragments of relatively small individual masses, and colliding fragments have typical relative velocities that are smaller than their individual escape velocities. When two particles stick, they are merged into a single spherical particle with the same momentum.

Because the initial conditions that give rise to a particular family are unknown, we must proceed by trial and error until the outcome matches the characteristics of the largest family member. To speed up this phase of the process, we do not integrate the system to late times using the *N*-body code but rather apply an iterative procedure (*9*, *17*) to identify this largest member. Except in the cases where its mass represents less than 10% of the target's mass, this procedure has been successful at predicting its actual characteristics.

Our first aim was to create a family with a fairly large mass ratio of the largest remnant to the parent body M_{lr}/M_{pb}. A good example of such a family is Eunomia. The list of family members is thought to be complete for bodies with diameters larger than 11 km; there are 110 Eunomia members larger than this value (*18*–*20*). The estimated diameter of the parent body

---

[1] Observatoire de la Côte d'Azur, B.P. 4229, 06304 Nice Cedex 4, France. [2] Physikalisches Institut, University of Bern, Sidlerstrasse 5, CH-3012 Bern, Switzerland. [3] Osservatorio Astronomico di Torino, Strada Osservatorio 20, 10025 Pino Torinese, Italy. [4] Department of Astronomy, University of Maryland, College Park, MD 20742–2421, USA.

*To whom correspondence should be addressed. E-mail: michel@obs-nice.fr

Fig. 1. Catastrophic disruption and gravitational reaccumulation. The picture shows a few snapshots of the time evolution of one of our *N*-body simulations. Each particle is shown to scale, assuming spherical shapes. The first frame on the left shows the initial condition, soon after the disruption of the parent body. The view size of this frame is 500 km, whereas the other frames (at times t = 0.55, 0.84, 1.68, and 8.38 hours) are 320 km. The rapid growth of a large remnant and of a complete hierarchy of fragment sizes is clearly apparent. While the largest remnant accretes fragments that are gravitationally bound, other bodies of different sizes diffuse in the surrounding space. Lighting conditions are arbitrary and are chosen for ray-tracing purposes only, and the point of view is at an angle of about 45° from the impact point.

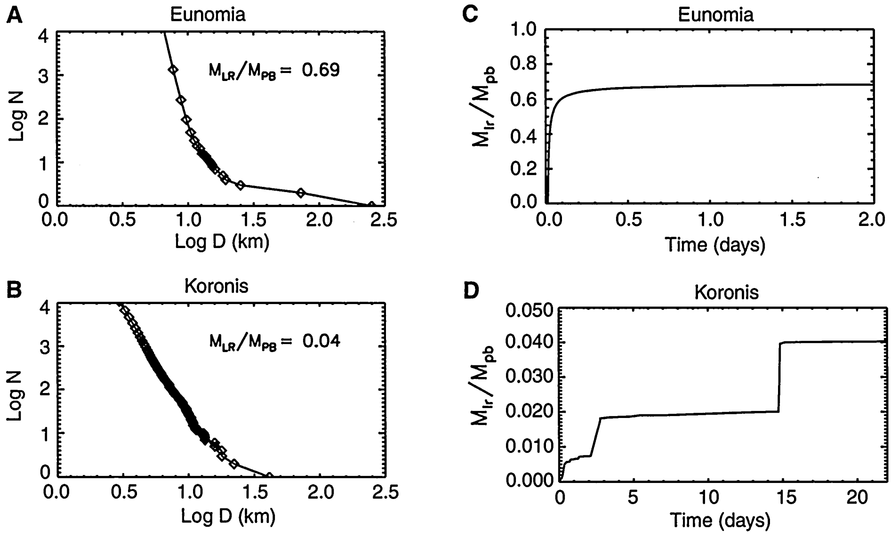

Fig. 2. (**A** and **B**) Cumulative diameter distributions (in km) of the fragments resulting from the two simulations of family formation in a log-log plot. (**C** and **D**) M_{lr}/M_{pb} as a function of time during the gravitational *N*-body phase. The names at the top of the plots correspond to the real family names; that is, these simulations were performed using a target with diameter and bulk density corresponding to those of the parent body of these families.

is 284 km (*21*) and M_{lr}/M_{pb} = 0.72. It has thus been defined as a partially disrupted family (*22*).

We performed several SPH simulations of the breakup of a 284-km-sized solid target represented by 10^5 SPH particles. Because the spectral properties of Eunomia members have features matching S type asteroids, the bulk density of the particles was assumed to be 2.7 g/cm^3 (*23*, *24*). From the particle masses and their assumed spherical shape, a particle radius of ≈3.07 km was estimated. Using the iterative procedure, a largest remnant with a mass (M_{lr}/M_{pb} = 0.70) close to the observed one (M_{lr}/M_{pb} = 0.72) can be produced by a projectile 48 km in diameter colliding at 6 km/s with an impact angle of 0°, which corresponds to a specific impact energy $Q = 8.7 \times 10^8$ erg/g (*25*). Both the value of the impact velocity and the size of the projectile are compatible with the mean collisional velocity between asteroids in the main belt and their collision rates (*26*, *27*). Other combinations of the collision parameters might equally be possible. It is important to stress that these impact conditions completely shatter the target down to the SPH resolution limit at the end of the fragmentation phase. In other words, we end up with as many fragments as initial SPH particles.

We then computed the gravitational evolution of this totally fragmented target with the *N*-body code. The reaccumulation of the largest fragment occurs immediately after the beginning of the simulation and its growth quickly stabilizes (Fig. 2C). Thus, even though the target is pulverized through crack propagation, the ejection velocities of most fragments are not high enough to let them get far from their initial positions before falling back together. After this initial collapse, the dominant body continues to accrete fragments at a slower rate. By the time its growth stops, 26% of the escaping mass is in single particles, and the remainder makes up a full size spectrum of well-separated rubble piles (Fig. 2A). Thus, our simulation shows that gravitational reaccumulation is at the origin of the formation not only of the largest remnant but also of the other large fragments with size above the simulation resolution. The extent of the reaccumulation is determined by the velocity field imposed by the collision physics on the individual fragments, and by the local mass density. Provided the shocks are well resolved, the latter is nearly independent of the degree of fragmentation and hence of the mass resolution (*28*).

The second and third largest fragments of the distribution have diameters equal to 36.1 km and 12.5 km, respectively, which is similar to the estimated diameters of the real Eunomia members (32.4 km and 14.3 km), if we neglect the two bigger Eunomia members identified as interlopers from their spectral properties (*20*). The thousands of other simulated fragments have diameters ranging from several tens of kilometers down to the resolution limit. This final configuration was measured 10.8 days after impact, beyond the time (roughly 1.7 days after impact) when there were no further statistically significant changes in the size distribution and ejection velocities (*29*).

Concerning the ejection velocities with respect to the parent body's center of mass, for the 1343 fragments of diameter larger than the mimimum size set by the resolution, the maximum speed is 0.725 km/s, the mean value is 0.091 km/s with a root mean square (rms) value of 0.075 km/s, and the speed of the largest remnant is ≈ 2.8×10^{-3} km/s (Table 1). This last value agrees with the estimated velocity of the real object (3.7×10^{-3} km/s) (*30*, *31*). Thus, after the complete shattering of the parent body, the gravitational reaccumulation process can lead to the formation of a large number of massive reaccumulated objects with ejection velocities high enough to create a dispersed family.

Our next goal was to create a family with a small M_{lr}/M_{pb}, such as the Koronis family. The completeness limit diameter of this family is 13 km, above which 55 members have been identified, and the most recent estimate of the parent body diameter is 119 km (*21*). For this family, M_{lr}/M_{pb} = 0.04, which indicates that it must have been created through a highly catastrophic event. Running several SPH simulations with 2×10^5 SPH particles, we found that a projectile 60 km in diameter colliding at 3.25 km/s with an angle of incidence of 75°, corresponding to $Q = 6.6 \times 10^9$ erg/g, leads to a mass ratio close to the real one and to a similar ejection velocity. As in the previous case, the fragmentation phase results in a completely shattered parent body composed of individual particles of radius 1.029 km. The gravitational reaccumulation phase, however, proceeds in this highly catastrophic event over a much longer time scale (≈15 days; Fig. 2D) than in the partially disrupted case discussed above. Fragments, which are ejected at higher speeds, must first be slowed down by gravity and brought back before reaccumulation can take place. In the end, reaccumulation leads in this case to $M_{\mathrm{lr}}/M_{\mathrm{pb}} = 0.04$, which is similar to the real value (Table 1), and to several other large fragments with diameters ranging from several tens of kilometers down to the resolution limit (*32*).

The ejection speeds of the resulting family members are accordingly much higher than those achieved by Eunomia members. In particular, the ejection speed of the largest remnant (of diameter 41.2 km in our simulation and similar to the observed value) is ≈0.076 km/s, which is again consistent with the estimated value of the real one (0.09 km/s). The mean ejection speed of the 21,199 objects with size greater than the resolution is 0.128 km/s, with a rms of 0.088 km/s.

Even though our simulations were not meant to reproduce perfectly the properties derived for the real families, it is instructive to compare both size distributions. This can be done by computing the slope of the cumulative size distributions in a log-log representation. For Eunomia (Fig. 2A), we obtain a slope of −4.9 ± 0.16, to be compared with the value of −4.40 ± 0.42 derived for the real family (*21*). For Koronis, we also obtain a steep size distribution (Fig. 2B) with a slope of −4.56 ± 0.02, whereas a slope of −2.55 ± 0.34 is estimated for the observed family (*21*).

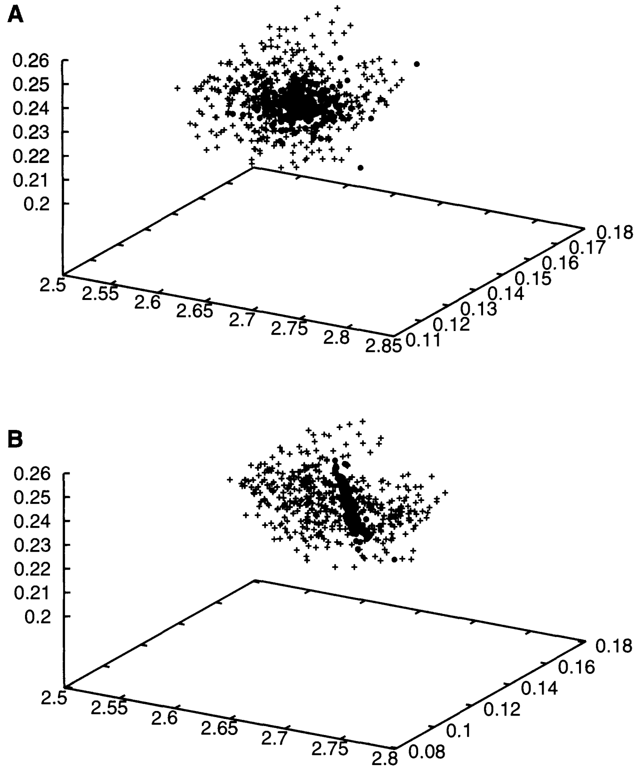

Fig. 3. Distribution in orbital proper element space [*a* (in AU), *e*, and sin(*I*)] of the real family members (crosses) and simulated families (circles) computed from Gauss equations. Different values of the parent body's true anomaly at impact f_0 and its sum with the argument of perihelion were used to sample the different shapes of the grouping in this space. In the case of Eunomia, the values $f_0 = 120°$ and $(f_0 + \omega) = 20°$ (**A**), and $f_0 = 175°$ and $(f_0 + \omega) = 50°$ (**B**), represent different possible shapes. For Koronis (**C**), the plot shows only the results using $f_0 = 120°$ and $(f_0 + \omega) = 20°$ (similar changes in shape are obtained with the other values used for Eunomia). For each simulated family, the number of fragments shown is equal to the number of identified real members. Fragments with diameter larger than the completeness limit are systematically included, and a random choice of other fragments with size greater than the SPH resolution is made. The dense grouping of each simulated family with respect to the real one suggests some strong diffusion processes acting on the proper elements of the real members. In particular, the tail at the rightmost end of the real Koronis grouping may be explained by a slow diffusion in semimajor axis and eccentricity resulting from the interplay between the Yarkovsky effect and the presence of high-order secular resonances (*40, 41*). This family may thus have already lost several members by this mechanism.

It has been pointed out (*33*) that families with a steep size distribution evolve collisionally toward a shallower distribution characterized by a slope that converges progressively to −2.5 (*34*). If we interpret the differences in slopes between the computed and real families as a consequence of subsequent evolution, the small difference for Eunomia indicates a young age for the family, assuming standard collisional erosion. Conversely, the larger difference for Koronis is consistent with the estimated old age of ≈1.5 billion years of the real family, based on crater counts of asteroid member Ida's surface (*35*). The original size distribution thus had time to become shallower as a result of collisional erosion.

The orbital dispersion of the fragments produced by the breakup can be computed by Gauss formulas, which relate fragment velocities to orbital elements. For each family, we used the estimated values of the barycenter semimajor axis, eccentricity, and inclination (*36*) with the Gauss formulas up to first order in eccentricity to compute for each member the distance of its orbital elements δa, δe, and δI from the barycenter of the family:

$$\begin{cases} \dfrac{\delta a}{a_b} = \dfrac{2}{n a_b \sqrt{1 - e_b^2}} [(1 + e_b \cos f_0) V_{\mathrm{T}} + e_b \sin f_0 V_{\mathrm{R}}], \\ \delta e = \dfrac{\sqrt{1 - e_b^2}}{n a_b} [\dfrac{e_b + 2 \cos f_0 + e_b \cos^2 f_0}{1 + e_b \cos f_0} V_{\mathrm{T}} \\ \qquad + \sin f_0 V_{\mathrm{R}}], \\ \delta I = \dfrac{\sqrt{1 - e_b^2}}{n a_b} \dfrac{\cos(\omega + f_0)}{1 + e_b \cos f_0} V_{\mathrm{W}}, \end{cases} \tag{1}$$

where V_{T}, V_{R}, and V_{W} are the components of the ejection velocity in the along-track, radial, and out-of-plane directions, respectively; n is the mean motion; f_0 is the true anomaly

Table 1. Comparison between observed properties (Obs.) and the results of our simulations (Sim.) for the two families considered. D_{pb} is the estimated diameter of the parent body (*21*). D_{lr} is the diameter of the largest remnant deduced from the albedo and magnitude for the observed one. V_{lr} is the largest remnant ejection speed. The values in the Obs.' columns are deduced from computed proper elements of the largest members and other approximations (*30, 31*).

Family	D_{pb} (km)	$M_{\mathrm{lr}}/M_{\mathrm{pb}}$		D_{lr} (km)		V_{lr} (m/s)	
		Obs.	Sim.	Obs.	Sim.	Obs.	Sim.
Eunomia	284	0.72	0.70	255.3	250.9	3.7	2.8
Koronis	119	0.04	0.04	41.2	41.2	90	76

of the parent body at the instant of the breakup; and ω is its argument of perihelion. Because these last two angles are not known, their values must be assumed. It has been shown (*37*) that the most sensitive angle is f_0. Assuming different values for this angle changes the shape of the cluster containing the family members in orbital element space. In other words, it defines whether the breakup generates a family that is spread in semimajor axis, in eccentricity, or in inclination. In the case of Eunomia, our simulation results in a tighter grouping of the fragments in the proper element space than is the case for the real family, regardless of the adopted value of f_0 (Fig. 3, A and B). This larger spreading can be explained by the existence of diffusion processes acting over the lifetime of the family (*38*, *39*). The presence of these diffusion processes is even more dramatically evidenced by the Koronis family (Fig. 3C). Koronis is located between the 5:2 and 7:3 mean-motion resonances with Jupiter, and in a region where high-order secular resonances are present. In particular, recent works (*40*, *41*) suggest that the tail at the rightmost end of the real Koronis grouping (Fig. 3C) can be explained by eccentricity pumping of family members along the line of some high-order secular resonances, whereas their semimajor axes drift as a result of the Yarkovsky thermal effect. Thus, dynamical mechanisms working in this region may well have modified the original shape of the family and even eliminated some of its initial members (*42*).

Our simulations have also indicated that the formation of small satellites about some members is a natural and frequent outcome of family-generating collisional events (*43*–*46*). To search for satellites, we have computed the orbital elements of all the fragments with respect to the largest remnant in each of the simulations (*47*). A satellite is defined as an object orbiting around the primary with an eccentricity smaller than 1 and a semimajor axis smaller than the Hill's radius of the primary (*48*) but a perihelion distance greater than the physical radius of the primary (Table 2). Almost all the satellites produced in our simulations evolve entirely inside the Hill's sphere of their primary. This is one of the required conditions for their stability.

Table 2. Number (N_b) of satellites of the largest remnant at the end of the simulations for the two families. The third column indicates the total number of satellites with orbits entirely inside the Hill's radius (R_H) of their primary. Q is the maximum distance to the primary of the satellite along its orbit. In the columns with $R > R_{min}$, only objects with radius greater than the minimum value R_{min} imposed by the resolution of our simulations have been considered. The last column gives the mass ratio of the largest satellite to the primary. The higher mass ratio in the case of Koronis can be explained by the already small value of the largest remnant mass (4% of the parent body mass).

Family	Nb total	Nb total $Q < R_H$	Nb $R > R_{min}$	Nb $R > R_{min}$ $Q < R_H$	M_{ls}/M_{prim}
Eunomia	421	398	43	42	7.3×10^{-5}
Koronis	170	165	52	51	0.02

References and Notes

1. P. Farinella, D. R. Davis, F. Marzari, in *Completing the Inventory of the Solar System*, T. W. Rettig, J. M. Hahn, Eds. (*ASP Conference Series 107*, Astronomical Society of the Pacific, San Francisco, CA, 1996), pp. 45–55.
2. Proper elements are quasi-invariants of motion, which are not affected by short-term perturbations. They are thus not supposed to change much over time, unlike osculating orbital elements.
3. V. Zappalà *et al.*, *Icarus* **116**, 291 (1995).
4. E. V. Ryan, H. J. Melosh, *Icarus* **133**, 1 (1998).
5. D. R. Davis *et al.*, *Icarus* **62**, 30 (1985).
6. C. R. Chapman *et al.*, in *Asteroids II*, R. P. Binzel, T. Gehrels, M. S. Matthews, Eds. (Univ. of Arizona Press, Tucson, AZ, 1989), pp. 386–415.
7. This idea had previously been suggested (*49*), and numerical simulations (*9*) had already shown that at least the largest family member had to be a bound aggregate. However, the formation of a full family by reaccumulation of smaller fragments remained to be demonstrated.
8. A rubble pile is a loose aggregate of fragments held together by gravity. Rubble piles have little to no tensile strength, so they can easily be torn apart by planetary tides.
9. W. Benz, E. Asphaug, *Icarus* **142**, 5 (1999).
10. ———, *Comput. Phys. Comm.* **87**, 253 (1995).
11. J. H. Tillotson, *General Atomic Report GA-3216* (General Atomic, San Diego, CA, 1962).
12. E. Asphaug, H. J. Melosh, *Icarus* **101**, 144 (1993).
13. W. A. Weibull, *Ingvetensk. Akad. Handl.* **151**, 5 (1939).
14. J. C. Jaeger, N. G. W. Cook, *Fundamentals of Rock Mechanics* (Chapman and Hall, London, 1969).
15. D. C. Richardson *et al.*, *Icarus* **143**, 45 (2000).
16. Because of the nature of the smoothing kernel in the SPH code, the initial conditions for the *N*-body code may contain some particles that overlap initially. These pairs are merged immediately if they are less than a few tens; otherwise, the radii of the particles are reduced (keeping the mass constant) until the number of overlaps drops below a few dozen.
17. This procedure is an iterative technique adapted from methods used in simulations of galaxy formation. First, the binding energy of all intact fragments with respect to the largest one, or, if it is too small, to the one closest to the potential minimum, is computed. This serves as a seed for nucleating the total bound mass. Unbound particles are discarded, and the center-of-mass position and velocity of the aggregate are computed. Unbound particles with respect to this new center are again discarded, and the procedure is repeated until no particles are discarded. After typically 5 to 10 iterations, convergence is achieved and a friends-of-friends algorithm is finally used to check that fragment members of this gravitationally bound aggregate are also close spatially. Dynamical parameters such as mass, position, and velocity are also determined for this gravitationally bound aggregate (*9*).
18. Some objects identified as asteroid family members may be interlopers; that is, asteroids classified as members by the standard identification techniques but not belonging to the set of fragments originating from the parent body. In the case of Eunomia, some of the largest members may actually be interlopers (*19*). In particular, the second and third largest members are certainly interlopers, because they display featureless spectra similar to those of C-type asteroids, in contrast with the other members, which have been characterized as S-type asteroids (*20*).
19. F. Migliorini *et al.*, *Icarus* **118**, 271 (1995).
20. D. Lazzaro *et al.*, *Icarus* **142**, 445 (2001).
21. P. Tanga *et al.*, *Icarus* **141**, 65 (1999).
22. F. Marzari, P. Farinella, D. R. Davis, *Icarus* **142**, 63 (1999).
23. M. Belton *et al.*, *Nature* **374**, 785 (1995).
24. P. C. Thomas *et al.*, *Icarus* **145**, 348 (2000).
25. The specific impact energy is defined by $Q = E/M$ (in erg/g), where E is the kinetic energy of the projectile and M is the mass of the target.
26. W. F. Bottke, M. C. Nolan, R. Greenberg, R. A. Kolvoord, *Icarus* **107**, 255 (1994).
27. P. Farinella, D. R. Davis, *Icarus* **97**, 111 (1992).
28. Several calculations using different resolutions confirm this, even in the most stochastic case (*32*). For the same reason, models of the disruption and reaccumulation of Comet Shoemaker-Levy 9 are insensitive to the number of particles as long as their number is large enough as compared with the final number of fragments (*50*).
29. We also checked that this result is insensitive to the adopted values of some free parameters, such as the integration step size.
30. Ejection velocities of real members were computed (*31*) using a rough estimate of the escape velocity of fragments and using Gauss formulas to convert proper elements into ejection velocities with respect to the family barycenter. Only the transverse component of velocity at infinity was then used to compute the magnitude of the ejection velocity, because it can be derived from the proper semimajor axis alone, which is supposed to be stable. However, even though proper eccentricity and inclination are more likely to be affected by dynamical diffusion processes, this may also hold for the proper semimajor axis of small members, for which the Yarkovsky thermal effect acts efficiently (*51*). Thus, the ejection velocities deduced for the real family members have to be interpreted with caution.
31. A. Cellino *et al.*, *Icarus* **141**, 79 (1999).
32. In order to check the sensitivity of the results on the SPH resolution, we ran a simulation using the same impact conditions but four times fewer particles (5×10^4) inside the target. Even though the gravitational phase in such a catastrophic regime includes some stochastic processes, because the reaccumulations of the largest members do not occur immediately but rather after the fragments have evolved under their mutual perturbations, we find statistically similar results, suggesting that the dynamics has been well captured.
33. F. Marzari, D. R. Davis, V. Vanzani, *Icarus* **113**, 168 (1995).
34. J. S. Dohnanyi, in *Physical Studies of Minor Planets*, T. Gehrels, Ed. (NASA SP-267, NASA, Washington, DC, 1971).
35. C. R. Chapman *et al.*, *Icarus* **120**, 77 (1996).
36. The barycenters of Eunomia (i) and Koronis (ii) are located at: (i) $a_b = 2.643$ astronomical units (AU), $e_b = 0.148$, $I_b = 13.1°$; (ii) $a_b = 2.876$ AU, $e_b = 0.048$, $I_b = 2.1°$.
37. V. Zappalà *et al.*, *Icarus* **124**, 156 (1996).
38. N. Murray, M. Holman, *Astron. J.* **114**, 1246 (1997).
39. A. Morbidelli, D. Nesvorný, *Icarus* **139**, 295 (1999).
40. D. Vokrouhlicky *et al.*, *Asteroids 2001 Abstr.* **4.21**, 225 (2001).
41. W. F. Bottke, D. Vokrouhlický, M. Brož, D. Nesvorný, A. Morbidelli, *Science* [tktk].
42. D. Vokrouhlický, M. Brož, P. Farinella, Z. Knežević, *Bull. Am. Astron. Soc.* **31**, 2403 (1999).
43. A previous numerical study of the initial stages of the expanding debris field resulting from the disruption of an asteroid had already suggested that reaccretion can produce asteroid satellites (*44*). Moreover, many two-body systems (binaries) have been observed (*45*), like the one involving the Koronis member Ida and its little moon Dactyl (*46*).
44. D. D. Durda, *Icarus* **120**, 212 (1996).
45. W. J. Merline *et al.*, *Nature* **401**, 565 (1999).
46. C. R. Chapman *et al.*, *Nature* **374**, 783 (1995).
47. Satellites of smaller fragments have also been identified in the two cases, but we leave a detailed analysis for future studies.
48. The Hill's radius is defined as $R_H = a_b \times (M_{lr}/3)^{1/3}$, where a_b is the distance to the Sun (in AU) of the primary that we fixed at the barycenter of the family,

and M_{tr} is the primary mass in solar mass units. Inside the Hill's sphere, the motion of the satellite is controlled mainly by its primary, and perturbations from the planets can be neglected.

49. C. R. Chapman, D. R. Davis, R. Greenberg, *Meteoritics* **17**, 193 (1982).
50. E. Asphaug, W. Benz, *Icarus* **121**, 225 (1996).
51. P. Farinella, D. Vokrouhlicky, *Science* **283**, 1507 (1999).
52. We thank A. Morbidelli for his suggestions and constructive comments on the manuscript. We are grateful to the LISA team of the Observatoire de la Côte d'Azur (OCA), who generously provided access to their four-processor COMPAQ DEC ALPHA workstation. Simulations were also partly made on the SIVAM four-processor COMPAQ DEC ALPHA of OCA. P.M. acknowledges financial support from the Action Thématique Innovante 2001 of the French Institut National des Sciences de l'Univers. W.B. acknowledges support from the Swiss National Science Foundation. P.T. has worked on this project while staying at the OCA, thanks to the H. Poincaré fellowship 2001. This paper is dedicated to the memory of P. Farinella, who was a main contributor to past research advances on the problem of collisions between asteroids.

8 August 2001; accepted 9 October 2001

Indication of Global Deforestation at the Cretaceous-Tertiary Boundary by New Zealand Fern Spike

Vivi Vajda,[1]* J. Ian Raine,[2] Christopher J. Hollis[2]

The devastating effect on terrestrial plant communities of a bolide impact at the Cretaceous-Tertiary boundary is shown in fossil pollen and spore assemblages by a diverse flora being abruptly replaced by one dominated by a few species of fern. Well documented in North America, this fern spike signals widespread deforestation due to an impact winter or massive wildfires. A Southern Hemisphere record of a fern spike, together with a large iridium anomaly, indicates that the devastation was truly global. Recovery of New Zealand plant communities followed a pattern consistent with major climatic perturbations occurring after an impact winter that was possibly preceded by global wildfires.

The abrupt replacement of a diverse plant community by one dominated by a few species of fern in numerous Cretaceous-Tertiary (K-T) boundary sites in North America (*1–5*) is compelling evidence that a giant bolide impact in the Northern Yucatan 65 million years ago (*6*) caused widespread and catastrophic disruption of terrestrial ecosystems. There has been little evidence of similar devastation in the Southern Hemisphere. Indications that the effects of the impact were less severe (*7*), however, are difficult to reconcile with knowledge that Australasian dinosaurs and marine reptiles suffered the same level of end-Cretaceous extinction as their northern cousins (*8*).

Pollen and spore assemblages from nonmarine coal and sandstone beds in the Moody Creek Mine section, West Coast, New Zealand (171°16′40″E, 42°23′18″S), let us reassess the effects of the bolide impact on terrestrial ecosystems in the Southern Hemisphere. Anomalous enrichment in iridium, chromium, cobalt, arsenic, and gold indicate that the section has an intact K-T boundary layer within a coal seam (Fig. 1). The iridium anomaly of 71 parts per billion (ppb) is the highest known from nonmarine rocks anywhere in the world [Web table 1 (*9, 10*)]. The boundary location is consistent with the last appearances of Late Cretaceous pollen species (*Tricolpites lilliei* and *Nothofagidites kaitangata*) in the underlying sample.

Our palynological study (*11*) is based on 30 samples spanning 2.1 m (Figs. 1 and 2). In this mire setting, these assemblages are considered to be reliable representations of the pre-impact local vegetation. The Late Cretaceous assemblages are diverse, with gymnosperms dominant, ferns abundant, and angiosperms common (mean values of 57, 25, and 14%, respectively). Gymnosperms increase to ~70% in the uppermost Cretaceous at the expense of ferns and angiosperms. The K-T boundary fern spike begins with an abrupt increase in ferns to 90% of the assemblage, mainly the form genus *Laevigatosporites*, but including the only common occurrence (8%) of sphagnum moss (*Stereisporites*). Gymnosperms are greatly reduced, and angiosperms disappear completely. In searches of more than 2000 specimens per sample, no angiosperm pollen was observed over an interval of 12 cm from the base of the 40-cm-thick fern spike. The fern spike is characterized by the successive dominance of different groups, such as ground ferns (*Laevigatosporites*, *Gleicheniidites*, and *Baculatisporites*) in the lower part [Web fig. 1 (*10*)] and tree ferns (*Cyathidites* and *Cibotiidites*) in the upper part. Modern relatives of these ground ferns are tolerant of open ground and acidic water-logged conditions, whereas modern tree ferns thrive in warm and humid conditions (*12*). There follows in the Moody Creek Mine succession a marked decline in ferns and a rise in gymnosperms, principally *Phyllocladidites mawsonii*. This pollen type is related to that of the extant conifer *Lagarostrobus franklinii*, which inhabits the cool-temperate rainforests of Tasmania (*13*). Angiosperms remain an insignificant component of the flora until 1.3 m above the K-T boundary. A short-lived recovery of ground ferns at the top of the fern spike may signal the first stage of regional climatic cooling, or it may be a localized phenomenon.

Identification of a similar succession of spore and pollen assemblages in a nearby marine K-T boundary section at mid-Waipara River, Canterbury (172°34′56″E, 43°3′44″S), indicates that the fern-to-gymnosperm succession reflects New Zealand–wide changes in vegetation through the K-T transition (Fig. 2). Further, although the spore and pollen records have been blurred by transport and mixing of terrestrial debris in this shallow marine setting, the well-defined boundary (*14*) and biostratigraphic control (*15, 16*) help constrain the duration of the Paleocene floral succession. General trends at mid-Waipara are similar to those reported from a marine section in Hokkaido, Japan (*17*), where the fern spike also separates mixed forest Cretaceous assemblages from gymnosperm-dominated Paleocene assemblages. The floral succession at Moody Creek Mine is similar to that in nonmarine K-T sections in North America, where the fern spike is made up of groups such as *Laevigatosporites* and *Cyathidiites* (*1, 3–5*). The North America fern spike also marks significant floral turnover from angiosperm-rich Cretaceous floras to gymnosperm-dominated ones (*2, 18, 19*).

Our results indicate that the devastation of forests after the K-T boundary impact was a global phenomenon. Even the geographically isolated vegetation of New Zealand, far from the impact site, was severely affected. We recognize five phases in the floral succession: (i) abrupt extinction or local disappearance of terrestrial vegetation due to prolonged darkness, freezing ground temperatures, possibly extensive wildfires, and acid rain (*20*); (ii) colonization of a waterlogged, acidic, cool landscape by a succession of moss and ground ferns; (iii) expansion of tree ferns in the upper part of the fern spike at both Moody Creek Mine and mid-Waipara (Fig. 2), indicating that a regional change to warm humid conditions followed earliest Paleocene cooling; (iv) decline in tree ferns before a long-term rise in cool-temperate gymnosperms, con-

---

[1] Department of Geology, Lund University, Tornavägen 13, SE–223 63 Lund, Sweden. [2] Institute of Geological and Nuclear Sciences, Post Office Box 30–368, Lower Hutt, New Zealand.

*To whom correspondence should be addressed: E-mail: vivi.vajda@geol.lu.se